Mon. Not. R. Astron. Soc. **000**, 1–13 (2012) Printed 31 January 2022 (MN LATEX style file v2.2)

Applying a one-dimensional PDR model to the Taurus molecular cloud and its atomic envelope

J. S. Heiner[1⋆], E. Vázquez-Semadeni[1]
[1] *Centro de Radioastronomía y Astrofísica (CRyA), Universidad Nacional Autónoma de México, C.P. 58190 Morelia, Michoacán, Mexico*

arXiv:1212.4171v1 [astro-ph.GA] 17 Dec 2012

ABSTRACT
In this contribution, we test our previously published one-dimensional PDR model for deriving *total* hydrogen volume densities from HI column density measurements in extragalactic regions by applying it to the Taurus molecular cloud, where its predictions can be compared to available data. Also, we make the first direct detailed comparison of our model to CO(1-0) and far-infrared emission.

Using an incident UV flux G_0 of 4.25 ($\chi = 5$) throughout the main body of the cloud, we derive total hydrogen volume densities of ≈ 430 cm^{-3}, consistent with the extensive literature available on Taurus. The distribution of the volume densities shows a log-normal shape with a hint of a power-law shape on the high density end. We convert our volume densities to H_2 column densities assuming a cloud depth of 5 parsec and compare these column densities to observed CO emission. We find a slope equivalent to a CO conversion factor relation that is on the low end of reported values for this factor in the literature (0.9×10^{20} cm^{-2}(K km s^{-1})$^{-1}$), although this value is directly proportional to our assumed value of G_0 as well as the cloud depth. We seem to under-predict the total hydrogen gas as compared to 100 μm dust emission, which we speculate may be caused by a higher actual G_0 incident on the Taurus cloud than is generally assumed.

Key words: ISM: molecules — ISM: atoms — ISM: clouds — ISM: individual: Taurus

1 INTRODUCTION

Molecular hydrogen is widely considered the key ingredient in star formation. However, on extragalactic scales it is only observed directly at higher densities or excitation conditions. Photodissociation regions (where molecular hydrogen is destroyed) are key to learning more about the molecular gas, because observable amounts of atomic hydrogen are produced in these regions.

The available literature on photodissociation regions (PDRs) is extensive. Early work includes Hollenbach et al. (1971) and Jura (1974) on the formation and destruction of molecular hydrogen, Glassgold & Langer (1975) on the appearance of C^+ and CO, and calculations on more atomic and molecular species by e.g. Black & Dalgarno (1977) and van Dishoeck & Black (1986). Recent years have seen the arrival of various publicly available computer models that aim to solve the detailed structure of PDRs for many atomic and molecular species, such as CLOUDY (Ferland et al. 1998), the Meudon PDR code (Le Petit et al. 2006), the KOSMA-τ code (Röllig et al. 2006) and the 3D-PDR code (Bisbas et al. 2012). A variety of such codes were compared and the results published by Röllig et al. (2007). For the focus of this work, we will limit our attention to atomic and molecular hydrogen (as well as, to a certain extent, carbon monoxide) in low density molecular clouds, since we aim to explore and provide an independent probe of total hydrogen volume densities as opposed to a detailed model of the internal structure that includes predicted line intensities of various species.

In lower-density, lower-radiation regimes, it is possible to derive total hydrogen densities using the relatively straightforward process of photodissociation of molecular hydrogen, which results in detectable atomic hydrogen emission, potentially on galactic scales. A detailed study of a one-dimensional approach to such photodissociation regions was carried out by Hollenbach et al. (1991), including calculations connecting gas densities with the incident UV flux, CO and 100 μm dust emission. Their results have been used to model the interstellar medium of external galaxies as well as the Milky Way.

Li et al. (2002) studied PDRs in what they called the intermediate regime, or $n \approx 500-5000$ cm^{-3} and $G_0 \approx 10-60$, in the L1204 and S140 regions. While they successfully predicted several atomic and molecular emission lines, they observed enhanced H_2 emission that could possibly be ex-

⋆ E-mail: j.heiner@crya.unam.mx

© 2012 RAS

plained by enhanced formation rates or weak shocks related to turbulent decay.

The notion that a large fraction of extragalactic atomic hydrogen in galactic disks is produced in PDRs has been around for quite some time (Allen et al. 1986, 1997; Smith et al. 2000; Heiner et al. 2011). Using PDR-produced atomic hydrogen, it becomes possible to calculate total hydrogen volume densities at selected positions across galactic disks using a simple approximate analytical one-dimensional PDR model (see also e.g. Higdon et al. 2011). The resulting densities are consistent with values expected for the diffuse interstellar medium. Corresponding molecular emission (CO) is found near higher (several hundred cm^{-3}) total hydrogen volume densities, although it should be noted that underexcited CO could still hide in relatively dense clouds. The densities obtained in this manner are also consistent with the (volumetric) Schmidt Law, linking the local star formation rate to the total hydrogen volume density (Heiner et al. 2010), at least in the power-law exponent.

However, so far this approach has not been compared directly to CO-derived molecular hydrogen gas contents in a detailed fashion. In order to do this, we turn to our own Galaxy to apply the one-dimensional PDR model to a molecular cloud that has densities in the range where this model can be expected to apply, namely below 10^4 cm^{-3}.

We selected the well-known and heavily-studied Taurus molecular cloud, part of the Perseus-Taurus-Auriga complex for this study. It has molecular gas densities of a few hundred cm^{-3} with denser clumps (for a recent comprehensive study, see e.g. Pineda et al. 2010) and is relatively quiescent in terms of star formation.

The atomic hydrogen in the Taurus area is considered to be connected to the molecular gas (Li & Goldsmith 2003). Several surveys of Taurus have been completed in the CO 1-0 line (Ungerechts & Thaddeus 1987; Narayanan et al. 2008) as well as a number of studies focusing on specific regions.

According to Ungerechts & Thaddeus (1987), the Taurus CO mass is of the order of 10^4 $\mathrm{M}_\odot$, depending on which parts of the complex are included (see also Pineda et al. 2010). Furthermore, clouds in the Taurus complex were found to have CO-derived masses approximately equal to their virial masses (Heyer et al. 1987). Abergel et al. (1995) compared the Taurus CO emission with IRAS far-infrared emission maps to conclude that the CO emission should trace at least 70% of the matter indicated by the 100μm emission, using the Ungerechts & Thaddeus (1987) maps. This makes Taurus a good candidate to compare the results of the simple one-dimensional PDR model to known molecular data, which will support the case for applying this model in the extragalactic case as well.

In the case of Taurus, then, we have a molecular cloud that is bathed in a photodissociating flux coming from the outside. We may assume that the molecular cloud is surrounded by an envelope of atomic hydrogen, that is either in the process of becoming molecular, or originates from photodissociated molecular hydrogen. Either way, this atomic hydrogen is part of the balance of photodissociation. Our study provides a starting point to further investigation of the atomic-to-molecular transition around molecular clouds in the context of the kinematics of the gas, as prompted by, e.g., the work presented by Ballesteros-Paredes et al. (1999) and Nguyen Luong et al. (2011).

The application of the simple one-dimensional PDR model includes an assumption about the details of the conversion of HI to H_2 and back, namely that (at least in the extragalactic case) the full integrated HI column can be assumed to be part of the process, minus a local background value. For an edge-on large-scale PDR, this assumption is likely to overestimate the HI column and therefore underestimate the related total hydrogen volume density. The reason for this is that the line of sight from the observer through the galaxy probes edge-on HI shells more or less parallel to the shell's surface, which would yield a higher column density than the column density seen at a right angle to the surface (assuming a shell that is thinner than it is wide). The true three-dimensional structure of the cloud remains unknown, which is especially true for the extragalactic case.

In our own Galaxy, Allen et al. (2004) used a limited velocity range dictated by the local molecular emission (for Maddalena's Cloud), an approach that we also adopt here. Under these assumptions, we can trivially calculate the fraction of the total HI column density that is included in the chosen velocity range. However, this in itself only hints at the fraction of HI that is part of the transition from atomic to molecular gas (and back).

Also, while Allen et al. (2004) applied the simple PDR model to Maddalena's Cloud in our own Galaxy, a detailed, spatially resolved application fell outside the scope of their work. With the application of this method to Taurus, then, we expand on their result. Consequently, this allows us to study the distribution of total hydrogen volume densities in the Taurus region. This distribution holds important clues to the dynamical state of the cloud.

This paper is structured as follows: First, we briefly review the theory behind the one-dimensional PDR model and how it can be applied to the case of Taurus. We then describe the archival data we used to explore the Taurus region. We discuss obtaining appropriate atomic hydrogen column densities, after which we present total hydrogen volume density maps of the main Taurus area. We then proceed to compare our results to CO emission data, as well as far-infrared data. We check our results for consistency with the Allen et al. (2004) calculations and discuss the values of the UV field suggested by our study. Finally we end with a summary of our conclusions.

2 A SIMPLE ONE-DIMENSIONAL PDR MODEL APPLIED TO THE MOLECULAR CLOUD-ATOMIC ENVELOPE INTERFACE

We use a straightforward one-dimensional plane-parallel PDR model that connects atomic hydrogen, molecular hydrogen (through the total hydrogen volume density), the incident UV flux and the local dust-to-gas ratio. For a more thorough description we refer to, e.g., Heiner et al. (2008). The final, approximate formula describing the photodissociation balance, which we employ here, is:

$$n = 106\ G_0 \left(\frac{\delta}{\delta_0}\right)^{-0.3} \left[\exp\left(\frac{N_{\mathrm{HI}}(\delta/\delta_0)}{7.8\times10^{20}}\right) - 1\right]^{-1}, \qquad (1)$$

where n is the total hydrogen volume density in cm^{-3} averaged along the line of sight through the cloud, G_0 is the incident UV flux and δ/δ_0 is the dust-to-gas ratio scaled to the

solar neighborhood value and $N_{\rm HI}$ is the (PDR-produced) HI column density in the direction of the incident UV flux. The exponent in δ/δ_0 is slightly different from the one that was used previously because it includes the improvements suggested by Heaton (2009).

The atomic hydrogen column density predicted by this approximate analytical model is scaled to fit the column densities produced by numerical PDR calculations presented by Kaufman et al. (1999), as described in Allen et al. (2004). It assumes that the formation and destruction of molecular hydrogen are balanced, at least when integrated through the gas cloud (Sternberg 1988). It provides an estimate of the total hydrogen volume density at the location where a certain HI column density is measured, neglecting the finer details of the formation and destruction of molecular hydrogen and other elements in order to focus on the direct, line-of-sight-averaged connection between atomic hydrogen and molecular hydrogen.

In the current context, $G_0 = 0.85\chi$ (Hollenbach & Tielens 1999), where G_0 is the incident radiation in units of the Habing flux (Habing 1968) and χ is in units of the Draine field (Draine 1978). These definitions of the radiation field and their relation are valid under the assumption of a cloud approximated by a semi-infinite slab, illuminated isotropically, with radiation therefore entering through 2π steradians. In the case of Taurus, it is not clear where the incident flux originates, and we approximate the ambient radiation field by adopting a constant value for it following Goldsmith et al. (2010). Equation (1) requires a single value for the incident flux, namely the one at the edge of the cloud. In our model, it is not necessary to know whether the radiation originates from in front of, or from behind the cloud. The value of n, however, is an average and includes all the hydrogen gas along the line of sight through the cloud. This includes the atomic hydrogen at the edge of the cloud as well as the molecular hydrogen further inwards. This average value may include clumped gas along the line of sight as well.

This model is thought to be most useful in the density range 10 cm^{-3} $\lesssim$ n $\lesssim$ 10^5 cm^{-3} and $G_0 \lesssim 100$ (Allen et al. 2004). The underlying assumption is that (a large fraction of the) measured HI column density is indeed produced by photodissociation due to the nearby source of UV flux. Trivially, the total hydrogen column density $N = n \times d_{\rm cloud}$ where $d_{\rm cloud}$ is the assumed cloud depth. Throughout this paper, n or N without subscript will refer to total hydrogen quantities, that is $N = N_{\rm HI} + 2N_{\rm H_2}$.

In the extragalactic case, one needs to identify patches of HI in column density maps that are suspected to be associated with central OB star associations as seen on far-UV images. The linear dimension of the PDR model is then taken to stretch on the plane of the sky from the central star cluster through the HI patch. From the projected angular separation, a linear distance and a corresponding incident flux on the location of the HI emission are then calculated. It is important to select a PDR that is seen approximately edge-on in order to be able to calculate the incident flux, although we will suffer from projection effects. While the HI column density is not measured in the direction from the star cluster through the HI patch, it is nevertheless assumed that the measured column density is an appropriate probe of the required column density, as we explained in the Introduction. Specifically, we refer the reader to Heiner et al. (2008), their Figure 4c, showing an idealized representation of the expected morphology. Formally, a spherical molecular cloud is assumed, or a tubular filament in the plane of the sky. A more thorough study of the projection effects on the measured HI column density in the extragalactic case falls outside the scope of this paper, and will be investigated in more detail in a future contribution.

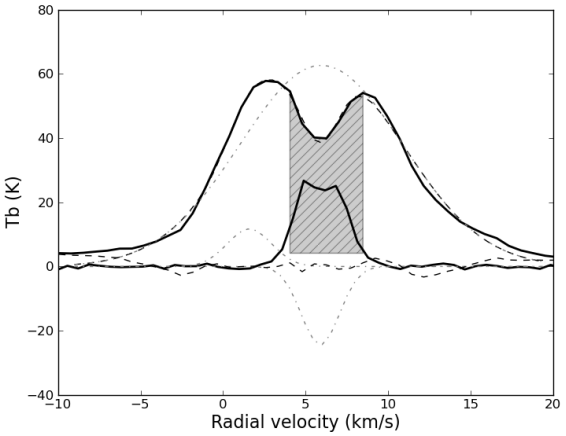


Figure 2. Sample profile from the GALFA HI datacube of Taurus. This particular profile shows a clear absorption feature as shown by three gaussians used to fit the line. Thick solid lines: HI profile and CO profile (multiplied by a factor of 5 for clarity). Dash-dotted lines: gaussian components of the fit. Dashed lines: fitted profile and residual. Gray area: section of the profile used to infer the local HI column density.

The applicability of the method is limited by the angular resolution of the images, meaning that only large-scale PDRs can be used (about 50-500 parsec separation). To apply this same method to PDRs in our own Galaxy, we take a slightly different approach. Instead of considering an edge-on PDR, we look at the PDR face-on. Here, we consider a uniform radiation field impinging on a known molecular cloud along the line of sight (with the radiation coming either from the direction of the observer or from behind the cloud), and attempt to isolate the photodissociated atomic hydrogen in front and behind the molecular cloud. The linear dimension of the PDR model is therefore perpendicular to the plane of the sky, and we can consider each pixel on the observed map individually, as long as the approximation of the incident radiation going along the line of sight holds. In principle, we should now measure the HI column density in the proper direction, although the three dimensional structure of the cloud remains unknown.

In this paper, we will compare our predicted column density $N_{\rm H_2}$ directly to the observed (velocity-integrated) $W_{\rm CO}$ CO(1-0) line emission. This CO emission is routinely converted to H_2 column densities using a constant conversion factor, otherwise known as $X_{\rm CO}$. In principle this quantity is defined only for an ensemble of molecular clouds on a galactic scale, but this conversion has also been applied on sub-kpc scales (Bigiel et al. 2008) or specific regions of our Galaxy (Abdo et al. 2010). The value of this so-called X-factor is thought to range between $0.9 - 4 \times 10^{20}$ cm^{-2} (K km s^{-1})$^{-1}$, but a Galac-

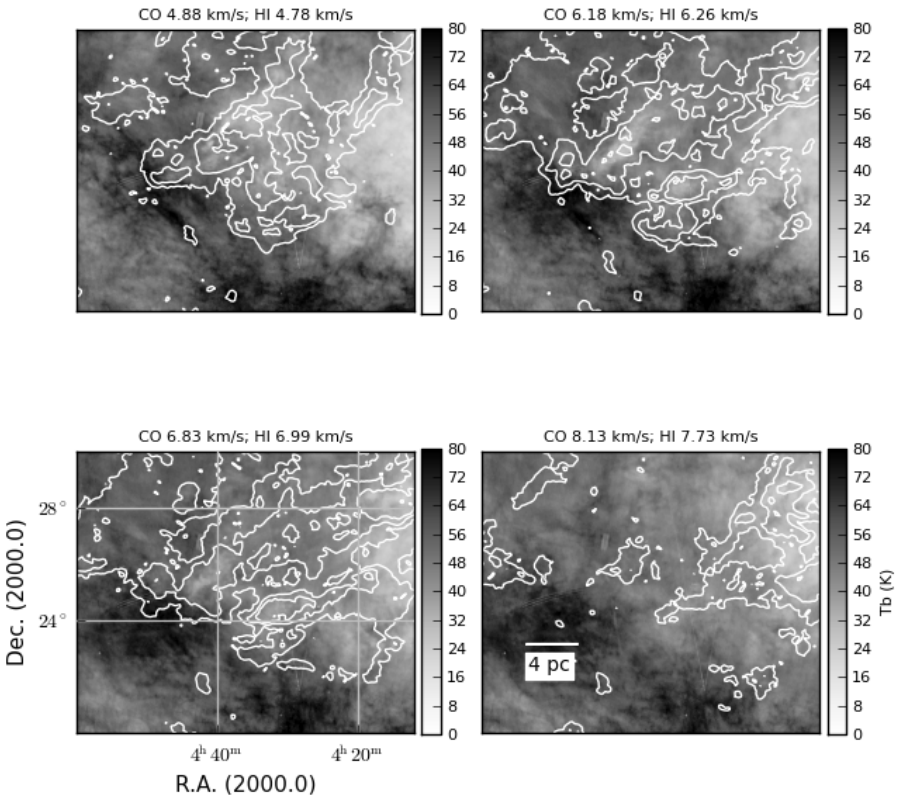


Figure 1. HI and CO emission near 5, 6, 7 and 8 km s^{-1}. CO contours are main beam brightness temperatures T_{mb} of 1, 3.5 and 6 K.

tic standard value in the same units is usually adopted for any galaxy in the absence of more direct measurements of this value. For example, Kennicutt (1998) used a factor of 2.8 $\times 10^{20}$ cm^{-2} (K km s^{-1})$^{-1}$ for a sample of 61 galaxies to derive H_2 column densities. The lower values have come from e.g. Digel et al. (1996) and the higher values from e.g. Draine et al. (2007).

For the purpose of our comparisons we will use the CO X-factor value adopted by Dame et al. (2001), namely 1.8 $\times$ 10^{20} cm^{-2} (K km s^{-1})$^{-1}$, since we use their CO data in this work. It should be noted that we use this value for reference purposes only, as it is helpful to plot this value as the slope in our figures comparing N_{H_2} to W_{CO}. At our parsec and sub-cloud scale a constant conversion factor should not be expected.

3 DATA AND PARAMETERS

For the one-dimensional PDR model described in Equation (1) we need the following parameters: the incident UV flux G_0, HI column densities, and the dust-to-gas ratio (scaled to the solar neighborhood) δ/δ_0. In addition we will be comparing our predicted densities to CO(1-0) and far-infrared (100 μm) derived H_2 column densities.

Following Goldsmith et al. (2010), we adopt a uniform incident χ of 5 (or $G_0 = 4.25$). They consider this value on the high end of the range based on a census of nearby B-stars, but they require at least a value this high to explain their observations. In our model, $n \propto G_0$, which means that underestimating G_0 also means underestimating the total hydrogen volume density.

We assume a solar dust-to-gas ratio ($\delta/\delta_0 = 1$). Fixing both the incident UV flux G_0 and the dust-to-gas ratio, appropriate for a relatively small region like the Taurus molecular cloud (as opposed to large-scale PDRs up to several hundred parsec across as investigated in the extragalactic case), means that the predicted total hydrogen density will vary with the HI column density only.

We use the 21-cm data from the GALFA-HI survey which has an effective beam size of 3.9 $\times$ 4.1 arcmin (Peek et al. 2011). We retrieved the data with a velocity separation of 736 m s^{-1}, ranging from a radial velocity of -10 km s^{-1} to 20 km s^{-1}, which is more than enough to include the Taurus molecular cloud at a radial velocity between 5 and 6 km s^{-1}.

Ballesteros-Paredes et al. (2009) modeled the main part of the molecular cloud as a 32 $\times$ 5 pc filament at a distance of about 145 pc, based on the distance measurements of Loinard et al. (2007) and Torres et al. (2007). We will adopt

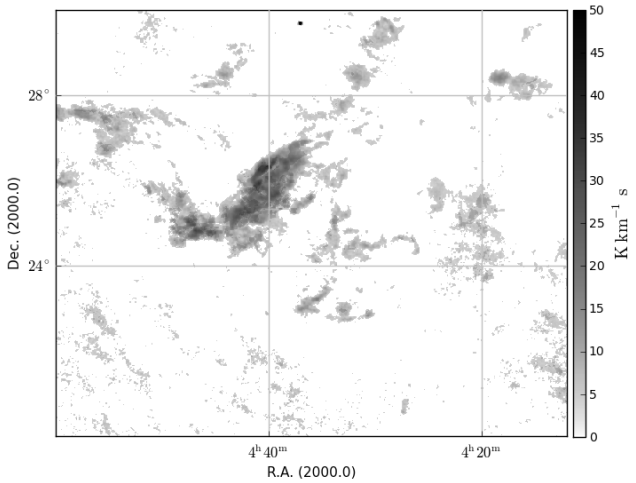


Figure 3. Map of the second derivative of the HI profiles indicative of the strength of HINSA features (integrated over a range of 5 to 7 km s^{-1}).

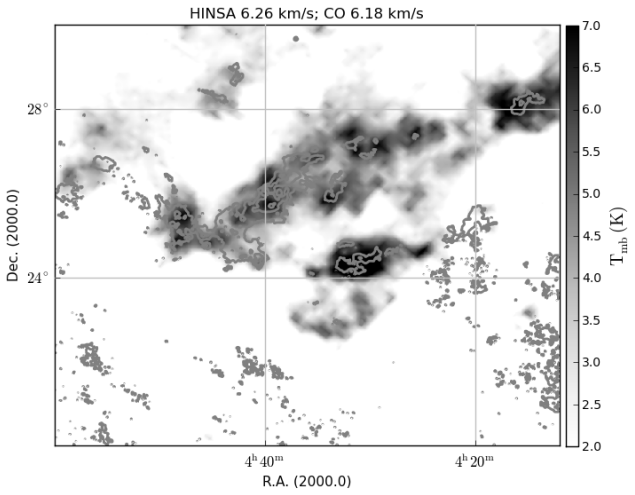


Figure 4. Contours of HINSA strength near 6 km s^{-1} on top of CO emission in grayscale. HINSA strength contours are 4, 12 and 20 K km^{-2} s^2

this model here. The actual distance does not influence our results.

We use the CO data of Taurus presented by Dame et al. (2001) for comparison. We reprojected it to the HI map first, but this results in an over-sampled CO map. We therefore smoothed the HI data to the CO resolution of 8.4 arcmin. Then, we regridded the data to a common grid; from 1 arcmin to 8 arcmin for the HI data by decimation, and from 7.5 arcmin to 8 arcmin by reprojection in the case of the CO data. This allows us to compare the data on a pixel-by-pixel basis.

Wolfire et al. (1993) investigated the expected CO line emission from GMCs and found that, for low UV fluxes ($1 < G_0 < 100$), the CO luminosity varies by only 10%. In order for the CO line profiles to appear smooth and centrally peaked, a large number of clumps need to be included in the (observing) beam. Since the Taurus CO line profiles indeed show this smooth shape, we believe assuming a uniform G_0 is justified.

We also used the 100 μm far-infrared dust map (temperature-corrected) produced by Schlegel et al. (1998) by extracting the general Taurus area from their all-sky map. The angular resolution is 6.1 arcmin, which we smoothed and regridded to 8 arcmin to compare the results.

4 OVERVIEW OF THE TAURUS REGION

In Figure 1 we show a number of CO/HI overlays that illustrate how the atomic and molecular gas in the Taurus area are intimately connected. Qualitatively, there is an anti-correlation between the CO and HI emission: the HI emission is clearly depressed in the areas where CO occurs. We aimed to locate parts of the Taurus cloud where our one-dimensional PDR model is likely to be applicable. In other words, we needed to find the parts on the map that seem to feature CO emission surrounded at the front and at the back by HI emission, along our line of sight. We then assumed that this HI emission is related to the balance of photodissociation described in the simple PDR model.

We show a fairly typical HI profile with the corresponding CO profile (artificially magnified by a factor of 5 for clarity) in an area dominated by CO emission in Figure 2. At first glance, this profile seems to show either two overlapping HI emission peaks, or perhaps a single peak with an absorption dip at the center. Both scenarios may point to the configuration we aimed to find: atomic hydrogen surrounding carbon monoxide, or atomic hydrogen tracing dense gas by displaying a (self-)absorption feature respectively. A good fit of this particular profile can be obtained using three gaussians (shown in the figure): a broad peak, small narrow peak and one gaussian representing absorption. Poorer fits are obtained using two or three positive-only gaussians (not shown). While many pixels in the datacube of the Taurus area can be fitted through this scheme, this in itself does not necessarily imply that absorption indeed occurs.

Li & Goldsmith (2003) conducted a survey of dark clouds in the Taurus/Perseus region in search of narrow absorption features in HI and OH emission. If the HI absorption feature is narrower than the CO linewidth, they call it HI narrow self-absorption (HINSA). They found that HINSA features correlate well with molecular tracers. For the Taurus area, they found HINSA column densities of about several times 10^{18} cm^{-2}, where it should be noted that measuring the HINSA feature does not necessarily mean fully filling the 'dip' in the line profile.

Indeed, the (negative) absorption gaussian profile in our Figure 2 corresponds to a column density about 30 times higher than 1×10^{18} cm^{-2}, which would lead us to overestimate not just the absorption, but also the HI emission grossly if we were to add both the positive broad gaussian as well as the absorption gaussian to infer a total HI column density. Therefore, we decided against fitting the HI

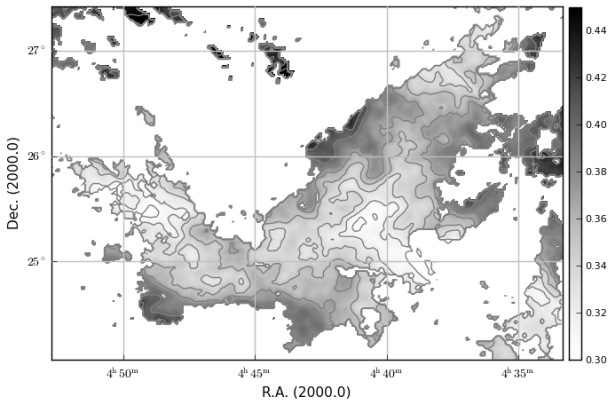


Figure 5. Fraction of the HI column density contained in our chosen velocity range of $4-8.5\mathrm{kms}^{-1}$ relative to the total HI column density over the range of -10 to 20 km s^{-1} (both background-subtracted).

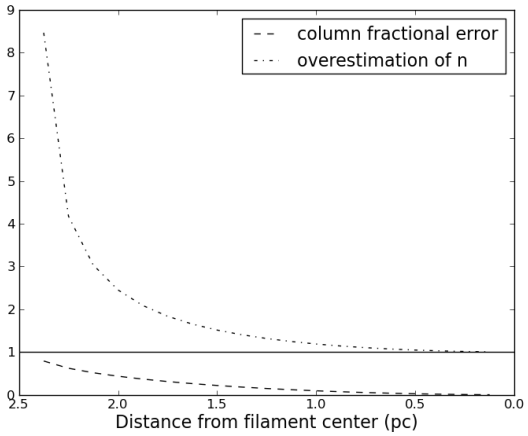


Figure 6. Estimated errors when the HI column is not taken exactly through the center of a filament, assuming a diameter of 5 parsec. Dashed line: fractional error in the HI column, 0 at the filament center and slowly increasing going outward. Dashed-dotted line: (fractional) overestimation of the calculated total hydrogen volume density. It slowly increases up to 50% at about 2 parsec away from the center and then starts to increase rapidly.

line profiles in the Taurus region as a way to identify areas where the simple PDR model can be applied.

Considering the comparatively low HINSA column densities found by Li & Goldsmith (2003), and in a more physically refined way by Krčo et al. (2008), relative to the overall HI column density, we finally elected to ignore the HINSA features for the purpose of calculating the HI column density related to the PDR. Instead, we opted to use the presence of HINSA only as an indication that our simple PDR model applies, independent of the presence of any CO emission.

As mentioned in the previous Section, we assume that the main Taurus molecular cloud can be pictured as a 32-by-5 pc filament. We can use this morphological information, specifically the filament depth, to estimate a total hydrogen column density from the volume densities obtained by our method. Choosing the appropriate line of sight is important, since due to the approximative nature of the model, it is possible for it to arrive at total hydrogen column densities that are less than the HI column density. It is therefore essential to make sure the model is applied to the proper regions. In the extragalactic case this is not a problem, since the columns are sufficiently deep not to get this close to the regime where the one-dimensional PDR approximation breaks down.

5 ATOMIC HYDROGEN COLUMN DENSITY

As mentioned in the previous section, even though we do not account for HINSA column densities in our HI calculations, we do use the presence of HINSA features to trace the pixels where we expect the simple PDR model to apply. It should be noted however that this does not mean that the model does not apply elsewhere in the cloud, so we do not necessarily trace all parts of the cloud where our model is applicable. To find HINSA, we use the method described in Krčo et al. (2008), where they show that HINSA is most easily seen in the second derivative of the HI line profile with respect to the velocity. The reason for this is that HINSA absorption features are typically Gaussian-like. Derivative functions of a Gaussian show a progressively stronger dependence on line width, making the narrow HINSA feature an easy-to-identify dominant feature in the second derivative as the broader overall profile is smoothed out. We can therefore construct a map that is indicative of the strength of the HINSA feature across the Taurus region, as shown in Figure 3. We integrated the second derivative velocity channels (in units of K km^{-2} s^2) over the range of 5 through 7 km s^{-1}. Then, we chose to select only those pixels with an integrated value of 4 K km^{-1} s or higher. We will refer to this integrated value as the HINSA strength. The resulting map shows the main Taurus area as well as features in other parts of the region. Figure 4 shows how the HINSA strength traces part of the Taurus CO emission.

The calculation of the atomic hydrogen column density (ignoring HINSA) requires additional assumptions. Given the very large width of the HI line ($\sim$ 20 km s^{-1}; Figure 2), it is natural to conclude that it originates from gas extending over much larger distances along the line of sight than the 5-pc assumed thickness for the cloud. Thus, in order to select only the atomic gas directly participating in the atomic to molecular transition into the cloud, we integrate only over the same velocity range that is spanned by the molecular gas at the position of the cloud, around 6 km s^{-1}, from 4.0 km s^{-1} to 8.5 km s^{-1} (gray area in Figure 2). For our background subtraction we simply took the minimum value in each profile over the range of -10 to 20 km s^{-1}, and we converted the observed velocity-integrated brightness temperature T_b to $N_{\rm HI}$ in the usual optically thick approximation by multiplying by 1.823×10^{18} cm^{-2} $\left(\mathrm{K\ km\ s^{-1}}\right)^{-1}$. Considering that Taurus is located at the Galactic anti-center, we do not expect any noticeable effects of galactic rotation on the radial velocities. A similar strategy to isolate the atomic hydrogen connected to a molecular cloud was used

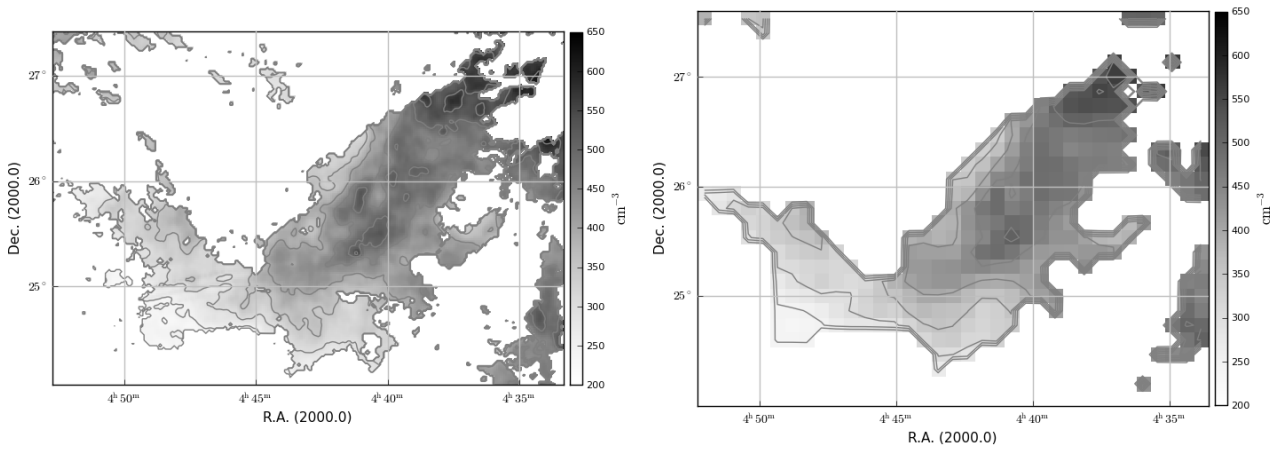


Figure 7. Total hydrogen volume densities in the main Taurus area, full (left) and decimated (right) version (used to compare with CO emission).

by e.g. Allen et al. (2004) and for Taurus itself by Hurwitz (1994), although the latter authors used a 4 km s^{-1} window centered on a 4 km s^{-1} radial velocity. Their HI column densities, only derived at selected positions, range from 1.6 to 2.7 $\times 10^{20}$ cm^{-2}. Despite the different central velocity, this is comparable to the low end of our values, which also include the higher HI column densities further away from the main Taurus region. Figure 5 shows the fraction of the total HI column density (background-subtracted) we recover in our chosen velocity range as compared to integrating over the full velocity range. Typically, this fraction is between 0.3 and 0.4.

We have also estimated the errors we make in the column and volume densities when assuming to be looking straight through a tubular filament. Our model assumes that the HI column is measured along the incident flux and, since we assume a uniform field impinging onto the surface of a filamentary (cylindrical) cloud, we should always measure the HI column straight through the center of the filament. In practice, we have a flat image and we do not know the exact filament center, so an error will be made when measuring the HI column directly from the map. Figure 6 shows the error made by taking the HI column off-axis, purely as a geometrical effect due to underestimating the path length through the filament. Obviously, the error close to the edge of the cloud is the largest, but the error in assumed HI column density is relatively modest for most of the distance between the center and the edge of the cloud. At 2 parsecs from the center (80% of the way) we would underestimate the HI column by about 50% and overestimate the total hydrogen volume density by about a factor two. Considering that the HINSA features seem to occur well inside the cloud (on the plane of the sky) and not too close to the edges of the main Taurus area, we conclude that at least in the main part of the molecular cloud these errors do not dominate our results.

6 TOTAL HYDROGEN VOLUME DENSITY MAPS

We calculated a total hydrogen volume density map at the native HI resolution and at a reduced resolution of 8 arcmin used to match the CO data. The full resolution map and the decimated map are shown in Figure 7. We stress that this calculation could be performed over a larger region. However, our model only works when we measure HI column densities close to the axis of the cloud filament – for lines of sight approximately perpendicular to the cloud surface. We assumed that cloud filaments are traced approximately by the level of HINSA strength.

The distribution of the calculated total hydrogen volume densities is shown in the histograms in Figure 8. In the left panel, the total hydrogen volume densities are shown for all pixels having a HINSA strength of at least 4. We find an average volume density of 436 cm^{-3} and a standard deviation σ = 129 cm^{-3}. If we look at specific regions of the cloud with strong CO emission (next section) we obtain a more limited range of values (right panel), with densities around 500 cm^{-3}. A total hydrogen volume density of about 430 cm^{-3} is consistent with the 405 cm^{-3} assumed by Ballesteros-Paredes et al. (2009), although theirs is an average for the whole cloud and does not include atomic hydrogen.

The shape of the density distributions is expected to be log-normal for isothermal flows, with a power-law tail for deviations due to gravitational collapse (Vázquez-Semadeni 1994; Passot & Vázquez-Semadeni 1998; Vázquez-Semadeni et al. 2008). More specifically, the shape of the density distribution should evolve based on the dynamics of the cloud, and the exact value of the power-law slope depends on the projection of the cloud against the sky as well (Kainulainen et al. 2009; Ballesteros-Paredes et al. 2011; Kritsuk et al. 2011). The left panel of Figure 8 shows a simple log-normal fit to the distribution. There is a hint of a power-law tail at the high-density end, whose existence would indicate that

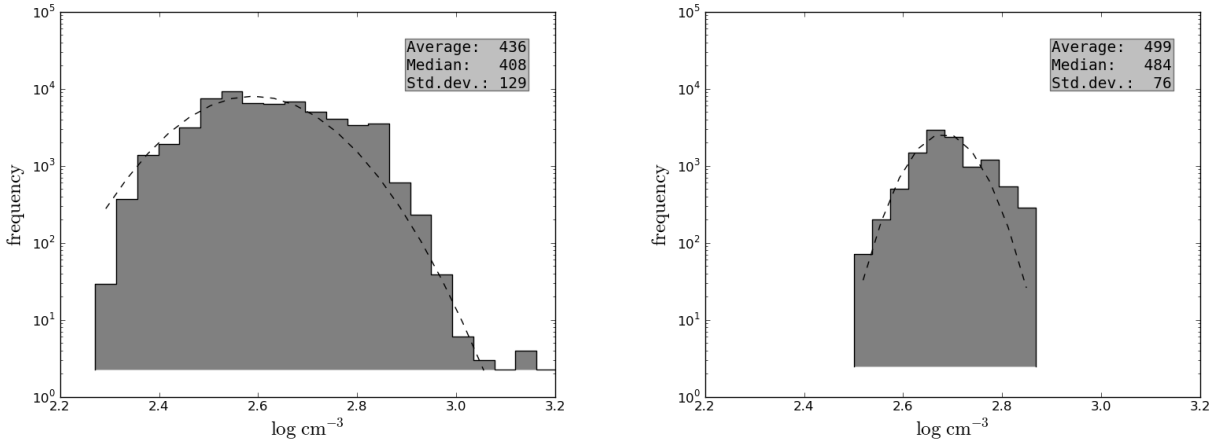


Figure 8. Left panel: Distribution of logarithmic total hydrogen volume densities using a HINSA strength threshold of 4., with a simple fit of a gaussian distribution. Note that this histogram is taken from the full-resolution density map. Right panel: Same, but only for regions 2, 3, 4, and 5 defined in Section 7.

the high density gas of the cloud is dominated by gravity. A more sophisticated determination of the HI column density as well as a more detailed knowledge of the radiation field G_0 would improve the analysis of the shape of the density distribution.

Again assuming an ellipsoidal shape for this region of Taurus, we arrive at a total hydrogen mass of $\approx 1 \times 10^4 M_\odot$, consistent with the CO mass in Ungerechts & Thaddeus (1987).

7 COMPARISON TO CO EMISSION

Assuming a cloud depth gives us the total hydrogen column density from the total hydrogen volume density and allows us to calculate an H_2 column density by subtracting the HI column density. This in turn can be compared to the CO emission from the Taurus molecular cloud. If the CO to H_2 conversion factor held down to the smallest scales, then the slope of an N_{H_2} vs. W_{CO} plot would yield this CO X-factor. In practice, we would expect this relation to break down in resolved clouds because of its local fluctuations. It is further known that the X-factor also varies on a cloud-by-cloud basis (e.g. Burgh et al. 2007). For these reasons, we caution that the comparison between our N_{H_2} and W_{CO} is for the purpose of a self-consistency check only.

In the left and right panels of Figure 9 we show the derived H_2 column density vs. W_{CO} for the pixels in the map with HINSA strength values of at least 4 and 15, respectively, using our adopted filament depth of 5 parsec. In the left panel we can distinguish roughly three features: a main cloud of points, a tail at the bottom (towards the right; more about this below) and another tail towards the upper-left part of the plot. The latter points disappear entirely for the higher HINSA strength threshold.

We also plot a linear correlation with a slope equal to the CO factor derived by Dame et al. (2001) on the basis of far-infrared imaging combined with HI maps, as well as dashed lines corresponding to twice and half this value, respectively. These dashed lines correspond also approximately to the reported range of the X-factor (cf. Section 2). We see that the points fall roughly in this range, but a least-squares fit of the points themselves, shown by the solid gray line, yields an even shallower slope of ~ 0.2 times the Dame et al. (2001) X-factor.

To investigate this correlation more closely, we defined five regions of interest based on the velocity-integrated local CO emission, as shown in Figure 10. These regions trace denser parts of the cloud as shown in the right panel of Figure 8. Figure 11 (left panel) shows the pixels of these five regions in the N_{H_2}-W_{CO} plane with different symbols. For each one of the regions, the slopes are shallow and lacking any real correlation, but cumulatively a slope is obtained of 0.9×10^{20} cm^{-2}(K km s^{-1})$^{-1}$, which is on the lower end of the range of usually quoted X-factors.

It can be seen that the derived N_{H_2} for the points in region 1, on the eastern tip of the main Taurus area, is consistently low when compared to the observed CO emission. We speculate that our filament depth assumption is off in this area. If the filament is curved towards or away from the observer, or if the cloud resembles less of a filament in this region, then we underestimate the filament depth and as a consequence we consistently underestimate the total hydrogen column density. If the cloud is twice as thick here than assumed, this would put the points in line with the other points. Indeed, Torres et al. (2009) note that Taurus may indeed be as deep as it is long in certain places (25 parsecs, according to their measurement).

Region 3 does not have many points left after imposing a HINSA-strength of 15. Region 4 centers on what is thought to be a parallel filament in the Taurus cloud and assuming the same filament depth results in column densities consistent with those found in the main part. The same can be said of region 5, which is at the north-west end.

Comparing with Figure 9 (left panel), we can see that in Figure 11 (left), the points in the upper-left corner have disappeared – they are not a part of the five selected regions in the main Taurus region. One possibility is that these points originate from a part of Taurus with a smaller column depth. Then our assumed column depth would be too large, lead-

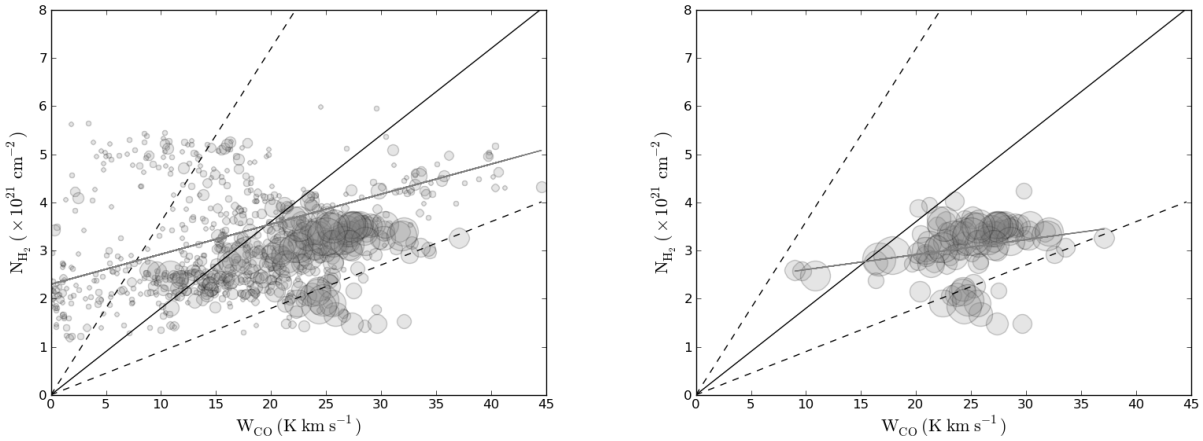


Figure 9. Comparison of predicted N_{H_2} vs. CO of the full map thresholded by HINSA map values of 4 (left panel) and 15 (right panel). The black solid line is the Dame et al. (2001) CO X-factor. The dashed lines represent twice and half the solid line's slope. The gray solid line shows a simple least squares fit to the data points. The size of the circles is proportional to the HINSA map strength.

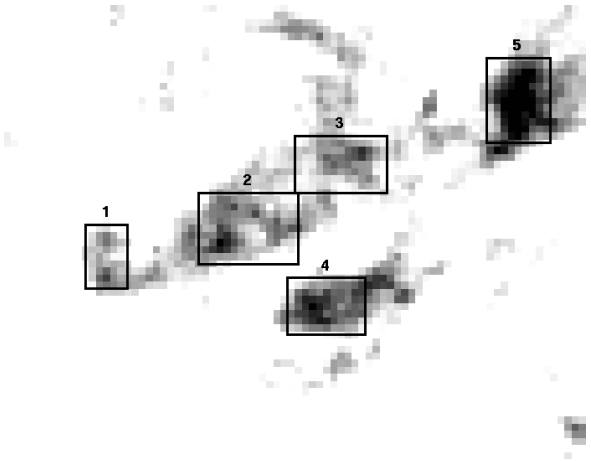


Figure 10. Regions of interest (boxes) displayed on top of a CO emission map.

ing us to overestimate total hydrogen column density and therefore also the molecular hydrogen column density. Alternatively, if the area to which these points belong is part of a filamentary structure, and has a column depth consistent with the one we assumed, the measured $N_{\rm HI}$ could be too far from the center of that filamentary structure, resulting in an underestimated HI column because of geometric considerations, as we showed in Figure 6, and therefore an overestimated total hydrogen volume density.

We show the effect of using a different cloud depth or a different χ in the right panel of Figure 11: a depth of 10 pc is used here or a χ of 10, both yielding the same result since n is linearly proportional to both of them. Recalling Equation (1) and $N = n \times d_{\rm cloud}$, it follows immediately that $N \propto G_0 d_{\rm cloud}$.

It is important to stress that our results are dependent on using an accurate estimate of the incident UV flux G_0. Since we used one constant value, we would expect that a better model of the radiation field would improve the accuracy of our results. Furthermore, we can only calculate an H_2 column density if we assume a certain cloud depth.

8 RANDOM MAPS

Because the distribution of points in Figures 9 and 11 exhibits significant amounts of scatter, it is useful to compare those results to cases in which the HI intensities in the maps are randomized, in order to see whether our results in those figures provide useful information. For this purpose, we considered the atomic hydrogen map randomized in two different ways. Then, we proceeded to calculate the total hydrogen column densities in the normal fashion, to see whether our results contain more information than these random cases.

First, we replaced all the pixels in the field by random values in the range of detected HI column densities. Based on the Taurus HI map we created a map with random column densities ranging from 2.5×10^{20} to 9.3×10^{20} cm^{-2}. These values are uniformly distributed within this range. Secondly, we took the observed HI column density map and randomly swapped pixel values. This way the global distribution of column density values is preserved, but the spatial image is destroyed.

Then, we calculated total hydrogen volume densities from both of these maps and compared the calculated H_2 column densities with the real CO emission map (Figure 12). The point sizes are proportional to the original (non-randomized) HINSA strength at each location. It can be seen that no clear correlation is left. The left panel plot (uniformly distributed $N_{\rm HI}$) shows more values towards the upper part of the plot than the right panel plot (shuffled $N_{\rm HI}$) because the distribution of the observed HI map is not uniform and contains fewer lower-end $N_{\rm HI}$ values. For comparison, see the same plot for the column densities calculated using original HI map as was shown in Figure 9. A much more restricted range of values is found here as well

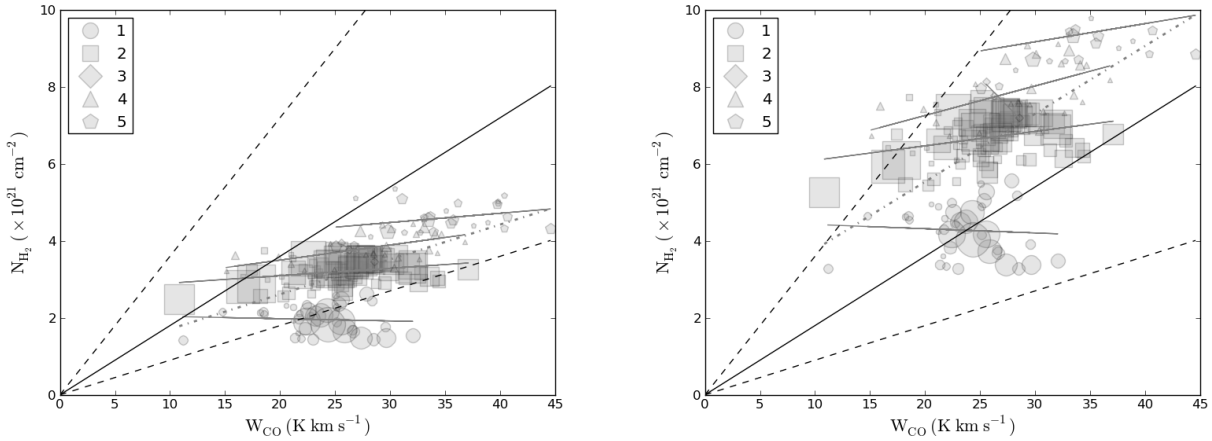


Figure 11. Comparison of predicted N_{H_2} vs. CO of the 5 selected regions as marked on Figure 10. A cloud depth of 5 parsec is assumed in the left panel. For each region a fitted least-square solid gray line is shown. The dash-dotted gray line is the fitted slope for all regions combined. The right panel shows the same plot, but assuming either a cloud depth of 10 parsec or $\chi = 10$, since the dependency of N on χ and cloud depth is the same. The size of the plot symbols is proportional to the HINSA map strength.

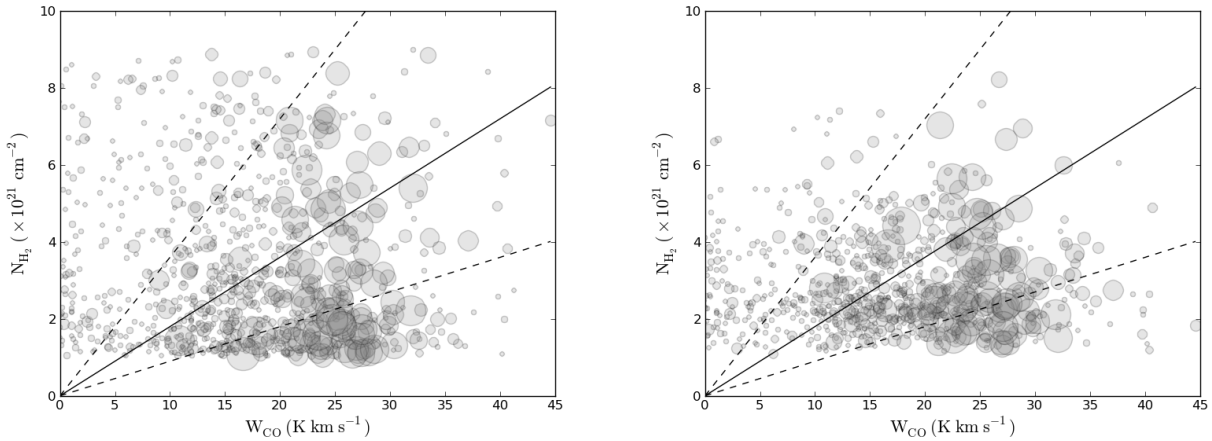


Figure 12. Left: N_{H_2} vs. CO from a map of random HI column densities. Right: N_{H_2} vs. CO from the GALFA-HI map with shuffled HI column densities. The circles are proportional to the HINSA strength. It can be seen that no clear correlation remains (cf. Figure 9).

as a better correlation, and therefore we conclude that our results provide real information.

9 COMPARISONS TO FAR-INFRARED EMISSION

Dust emission in the far-infrared has been found to correlate well with the total hydrogen column density. Dame et al. (2001) used the Schlegel et al. (1998) IRAS 100 μm to calculate the CO X-factor in our own Galaxy. To this end, they calculated the ratio between the atomic hydrogen column density and the 100 μm emission in regions free of CO(1-0) emission. The resulting ratio, 0.9×10^{20} cm^{-2}/(MJy sr^{-1}), (with an estimated uncertainty of 50%) can then be used to calculate the total hydrogen column densities in the regions with CO(1-0) emission which in turn leads to the calculation of the CO X-factor. It should be noted that while Dame et al. (2001) allowed for local variations of this 100 μm conversion factor, we adopt their globally averaged ratio here.

Abergel et al. (1995) compared the far-infrared emission of Taurus to CO emission and found that they correlate well globally. They estimate that at least 70% of the 100 μm-traced matter is traced by CO(1-0) emission as well. In other words, a bit more gas should be traced by 100 μm emission than by CO(1-0) in the Taurus region. For reference, we plot the HINSA strength contours on top of the FIR map in Figure 13 (cf. Figure 4). It can easily be seen that the FIR map and the CO map are qualitatively very similar in the densest regions. However, the infrared map shows additional diffuse structure not present in the CO map, consistent with the notion that the far-infrared continuum traces the total hydrogen gas rather than only the molecular gas.

We compare our results to the same (temperature-corrected) far-infrared map for completeness. A plot of this comparison is shown in the left panel of Figure 14. A cloud

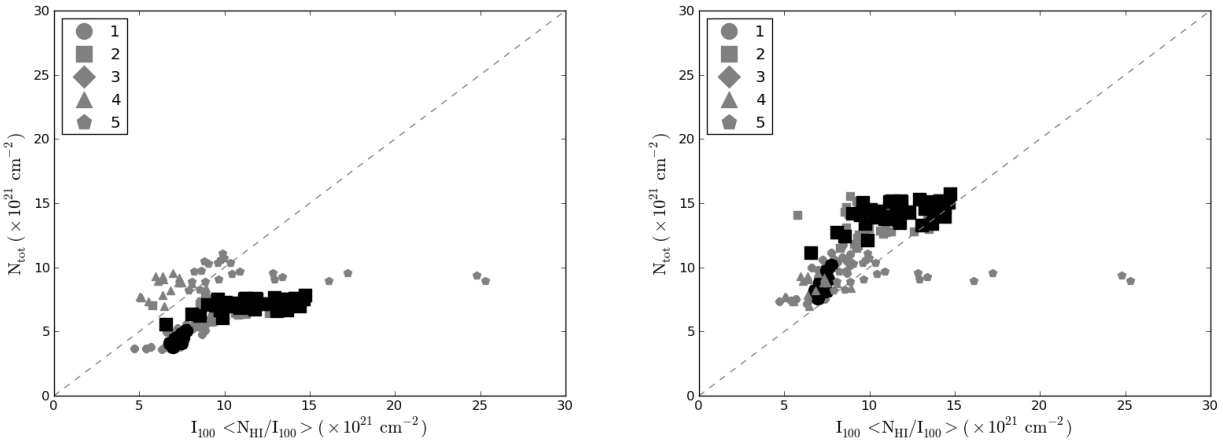


Figure 14. Left panel: N_{tot} (our method) vs. N_{tot} (100μm), with a 1-to-1 line for comparison using $< N_{HI}/I_{100} >= 0.9 \times 10^{20}$ cm^{-2}/(MJy sr^{-1}). The gray dots have a HINSA strength between 4 and 15; the black dots have a HINSA strength above 15. The latter can be seen to under-predict the total gas column densities as compared to the 100μm-predicted ones. Additionally, the same regions as marked in Figure 10 are marked. Right panel: same plot but the N_{tot} values of regions 1 and 2 have been artificially multiplied by 2.

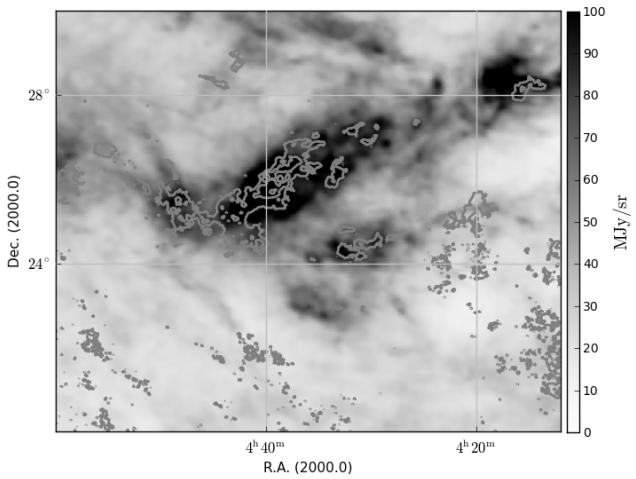


Figure 13. Contours of HINSA strength on top of the (temperature-corrected) 100μm map. HINSA strength contours are 4, 12 and 20 K km^{-2} s^2

depth of 5 parsecs is assumed as before. The FIR map was smoothed and reprojected to the same resolution as the CO map, namely 8 arcmin. The gray pixels correspond to a HINSA strength of 4 to 15; the black pixels to a HINSA strength of 15 and above, and additionally the same regions as marked in Figure 10 are indicated. There is a feature at the highest values of the 100 μm emission that is caused by a single source in the north-west part of the map (region 5) that partially overlaps with a HINSA detection. This explains the outlying points on the right-hand side of Figure 14.

It can be seen that the pixels corresponding to the higher HINSA strength are mostly confined to a single area in the plot (and regions 1 and 2). If we assume that the higher HINSA strength corresponds to a better applicability of our model, then this suggests that the model is underestimating the total hydrogen column density somewhat (the black pixels indicating a HINSA strength of 15 are predominantly situated below the 1-to-1 correlation line). A possible explanation of this deficiency would be that we have underestimated the column depth in region 1 and underestimated G_0 in region 2, both by a factor ~ 2 (note that N is linearly proportional to both column depth and G_0). The right panel of Figure 14 shows the result of multiplying our $N_{\rm H_2}$ by a factor of 2 in these regions. A tighter correlation is obtained in this case. (See also the discussion of the radiation field in Section 10.)

Even though the comparison of our method to far-infrared emission shows a clear structure, if we conservatively estimate our results to have an uncertainty comparable to the infrared method, namely 50%, the correlation is significantly degraded. We expect the derived total hydrogen volume densities to have the same or better uncertainties than the ones in the nearest extragalactic case, namely M33 (Heiner et al. 2011). The same range of values is obtained with our method as with the far-infrared method, meaning that both methods yield consistent results. In order to obtain better statistics a wider range of molecular clouds will need to be investigated in a similar fashion, both lower density as well as higher density clouds up to the applicability limit of $\sim 10^4$ cm^{-3} total hydrogen density.

10 CHARACTERIZING THE RADIATION FIELD IN TAURUS

Considering the relatively low implied H_2 column densities that we found in Taurus, we will discuss in this section the possibility of a stronger UV radiation field than we assumed. A stronger field would increase our inferred H_2 column densities.

10.1 PDR model comparison

Allen et al. (2004) presented calculations from a model of a one-dimensional plane-parallel PDR and how CO and HI emission relate to the incident flux G_0 and the total hydrogen volume density: Their Figures 1 and 2 provide diagnostic diagrams predicting a limited range of G_0 and n given an HI column density and CO intensity. Their work was an extension of the modeling done by Kaufman et al. (1999) that solved the chemistry, radiative transfer and thermal balance of one-dimensional PDRs. The Allen et al. (2004) results predict that the CO emission at the expected density of the Taurus region is in the regime where this emission is only very weakly dependent on the incident UV flux. Allen et al. (2004) compared their calculations to the overall characteristics of G216-2.5 (Maddalena's Cloud). We will now do the same for the Taurus area.

Taking the average CO emission over the full map yields $\langle W_{\rm CO}\rangle = 20.3$ K km s^{-1}. The average HI column density in the Taurus area in our selected velocity range is $\langle N_{\rm HI}\rangle = 5.7\times10^{20}$ cm^{-2}. Intersecting the values of $\langle W_{\rm CO}\rangle$ and $\langle N_{\rm HI}\rangle$ in Allen et al. (2004), their Figure 2, implies $G_0 \approx 6$ and a total hydrogen volume density of several hundred cm^{-3}. Computing the HI column density over a broader velocity range would raise the HI column density, implying a higher incident UV flux if n is fixed.

Figure 20 in Hollenbach et al. (1991) provides an additional way to infer G_0 from the total hydrogen volume density and the ratio $W_{\rm CO}/I_{100}$. Taking the average 100 μm emission in the Taurus area map of 40 MJy sr^{-1} we obtain $\langle W_{CO}\rangle/\langle I_{100}\rangle = 0.5$, which for volume densities of several hundred cm^{-3} implies $G_0 \gtrsim 10$.

The above discussion suggests that G_0 is in the range of 1 to perhaps several times 10. We consider this quite realistic, considering the extragalactic case – for example see the range of G_0 values obtained in M33 (Heiner et al. 2011). All that is needed is a cluster of a few dozen O or B stars within a few hundred parsecs distance (further than our own distance from Taurus) and a sufficiently clumpy interstellar medium to let the UV radiation penetrate.

10.2 Far-ultraviolet emission

A far-ultraviolet map of the Taurus region was presented by Lee et al. (2006), although the emission is comparatively faint ($\chi \approx 0.2$). They argue that the observed FUV intensity comes mainly from foreground radiation while radiation at the back of the cloud is blocked. Far-infrared emission should not be blocked, potentially providing an alternative measure of the UV field, but they point out that the relationship between $I_{\rm FUV}$ and $I_{100\mu\rm m}$ should deviate from a simple linear relationship in optically thick regions (such as Taurus). Such a linear relationship was proposed by Haikala et al. (1995), who provide their own estimate of the interstellar radiation field (see also Murthy & Sahnow 2004).

It is still instructive to convert the 100 μm image to an equivalent map of χ (the far-ultraviolet flux scaled by their interstellar radiation field value) using the linear relation from Haikala et al. (1995). The conversion with scaling becomes:

$$\chi = (128\ I_{100} - 264)\ /\ 6490, \qquad (2)$$

where χ is in equivalent dimensionless units of the usual χ since it was scaled to the interstellar radiation field value in the solar neighborhood. Scaling the 100 μm image in this fashion yields values up to $\chi = 3$, below our assumed $\chi = 5$. However, Figure 6 of Murthy & Sahnow (2004) shows the correlation between $I_{\rm FUV}$ and I_{100} for a broader range of values. It can be see that the inferred values of χ can be several times higher because of significant scatter in the correlation for values similar to the ones found in the Taurus area.

11 CONCLUSIONS

We used a simple one-dimensional PDR model to predict total hydrogen volume densities from HI column densities in the Taurus molecular cloud in regions with strong HI narrow self-absorption (HINSA). As Allen et al. (2004) noted, this procedure is primarily of use in the extragalactic case. However, it is important to test the method by applying it locally in our own Galaxy in order to validate the extragalactic results. To this end, we selected atomic hydrogen column densities from a limited range of velocities around the main molecular cloud radial velocity (ignoring HINSA corrections to the column densities).

The obtained total hydrogen volume densities appear to follow a log-normal distribution, potentially with a power-law tail at the high density end. Our method provides a promising tool to obtain the probability density function of the volume density of the gas in molecular clouds. We find an average total hydrogen volume density of 436 cm^{-3} (σ = 129 cm^{-3}) on the basis of pixels selected for HINSA features.

For the first time, we make a direct detailed comparison between our PDR-based method and CO-derived column densities (cf. Allen et al. 2004) as well as far-infrared-derived column densities. We found a correlation between $N_{\rm H_2}$ and $W_{\rm CO}$ with a cumulative slope of 0.9×10^{20} cm^{-2}(K km s^{-1})$^{-1}$, implying a relatively low value of the CO to H_2 conversion factor, at least when the full ensemble of data points is considered (individual parts of the Taurus cloud essentially show no correlation. However, assuming that the far-infrared emission is a good tracer of the total gas, our method yields lower total hydrogen column densities as compared to the column densities implied by the far-infrared emission, at least for higher values of the HINSA strength. There are three ways in which our total hydrogen column densities can be made larger: using a larger cloud depth, a higher incident UV flux G_0, or a lower HI column density (obtained by narrowing the velocity range of atomic hydrogen associated to Taurus).

We adopted $\chi = 5$ ($G_0 = 4.25$) from Goldsmith et al. (2010), although in line with their findings, this seems to be the lowest value for the UV radiation field that fits the observations. Twice this value might yield better results. We conclude, based on our results and the available literature, that a higher G_0 of at least 10 in the general Taurus area would be expected.

In the case of the central region of Taurus, it appears that all the gas mass is accounted for (since our results are consistent with both CO and FIR observations), unless the true G_0 pervading the molecular cloud is, unexpectedly,

at least several times higher than previously assumed. We might expect to find hidden 'dark' gas based on the work by Wolfire et al. (2010), or the observations of galactic supershells by Dawson et al. (2011). The parts of the Taurus area where we applied the plane-parallel PDR model were not CO-selected, but rather by the presence of HINSA; however, all selected areas do have detectable CO emission. One could assume that molecular gas not traced by CO is present in the atomic hydrogen layer surrounding the CO cloud, but the results of our method show no evidence of this in the form of predicted total hydrogen column densities consistently higher than those inferred by CO emission or infrared emission. Molecular gas not traced by CO could still be present in the areas directly surrounding Taurus, further away from the CO cloud on the plane of the sky. However, the lack of better information about the detailed UV radiation field in the Taurus region prevents a thorough search at this time. It would be of interest to apply the same model to similar clouds in our Galaxy with hints of 'dark' gas that is not traced by CO or where higher X-factors have been inferred.

Assuming a consistent relation between our inferred molecular gas versus the CO-implied gas, we speculate that the eastern tip of the Taurus cloud has twice the thickness of the main area, independent of what thickness is adopted or will be found for the main area.

The results of this work could be improved through a combination of cloud depth information to aid the direct comparison to CO (anticipating e.g. the Gould Belt Distance Survey, Loinard et al. 2011) and a more sophisticated way to calculate local (related) HI column densities. More accurate HI column density measurements would require, for example, a way to distinguish foreground and background HI emission from emission from the molecular cloud, if we could find out more about the local velocity and temperature structure.

Going forward, we expect to be able to use the simple PDR model in future work as a tool for investigating the atomic-molecular transition in molecular clouds.

ACKNOWLEDGMENTS

JSH acknowledges constructive comments from Ron Allen about the application of the simple PDR model and from Laurent Loinard about the morphology of the Taurus molecular cloud that helped improve the results. JSH is supported by CONACYT grant 102488 to EVS. We thank the anonymous referee for suggestions that improved the clarity of this work, particularly in terms of clarifying the differences between the Galactic and the extragalactic case.

REFERENCES

Abdo A. A. et al., 2010, ApJ, 710, 133
Abergel A., Boulanger F., Fukui Y., Mizuno A., 1995, A&AS, 111, 483
Allen R. J., Atherton P. D., Tilanus R. P. J., 1986, Nature, 319, 296
Allen R. J., Heaton H. I., Kaufman M. J., 2004, ApJ, 608, 314
Allen R. J., Knapen J. H., Bohlin R., Stecher T. P., 1997, ApJ, 487, 171
Ballesteros-Paredes J., Gómez G. C., Loinard L., Torres R. M., Pichardo B., 2009, MNRAS, 395, L81
Ballesteros-Paredes J., Hartmann L., Vázquez-Semadeni E., 1999, ApJ, 527, 285
Ballesteros-Paredes J., Vázquez-Semadeni E., Gazol A., Hartmann L. W., Heitsch F., Colín P., 2011, MNRAS, 416, 1436
Bigiel F., Leroy A., Walter F., Brinks E., de Blok W. J. G., Madore B., Thornley M. D., 2008, AJ, 136, 2846
Bisbas T. G., Bell T. A., Viti S., Yates J., Barlow M. J., 2012, MNRAS, 427, 2100
Black J. H., Dalgarno A., 1977, ApJS, 34, 405
Burgh E. B., France K., McCandliss S. R., 2007, ApJ, 658, 446
Dame T. M., Hartmann D., Thaddeus P., 2001, ApJ, 547, 792
Dawson J. R., McClure-Griffiths N. M., Kawamura A., Mizuno N., Onishi T., Mizuno A., Fukui Y., 2011, ApJ, 728, 127
Digel S. W., Grenier I. A., Heithausen A., Hunter S. D., Thaddeus P., 1996, ApJ, 463, 609
Draine B. T., 1978, ApJS, 36, 595
Draine B. T. et al., 2007, ApJ, 663, 866
Ferland G. J., Korista K. T., Verner D. A., Ferguson J. W., Kingdon J. B., Verner E. M., 1998, PASP, 110, 761
Glassgold A. E., Langer W. D., 1975, ApJ, 197, 347
Goldsmith P. F., Velusamy T., Li D., Langer W. D., 2010, ApJ, 715, 1370
Habing H. J., 1968, Bull. Astron. Inst. Netherlands, 19, 421
Haikala L. K., Mattila K., Bowyer S., Sasseen T. P., Lampton M., Knude J., 1995, ApJL, 443, L33
Heaton H. I., 2009, ApJ, 694, 978
Heiner J. S., Allen R. J., Emonts B. H. C., van der Kruit P. C., 2008, ApJ, 673, 798
Heiner J. S., Allen R. J., van der Kruit P. C., 2010, ApJ, 719, 1244
Heiner J. S., Allen R. J., van der Kruit P. C., 2011, MNRAS, 416, 2
Heyer M. H., Vrba F. J., Snell R. L., Schloerb F. P., Strom S. E., Goldsmith P. F., Strom K. M., 1987, ApJ, 321, 855
Higdon J. L., Higdon S. J. U., Rand R. J., 2011, ApJ, 739, 97
Hollenbach D. J., Takahashi T., Tielens A. G. G. M., 1991, ApJ, 377, 192
Hollenbach D. J., Tielens A. G. G. M., 1999, Reviews of Modern Physics, 71, 173
Hollenbach D. J., Werner M. W., Salpeter E. E., 1971, ApJ, 163, 165
Hurwitz M., 1994, ApJ, 433, 149
Jura M., 1974, ApJ, 191, 375
Kainulainen J., Lada C. J., Rathborne J. M., Alves J. F., 2009, A&A, 497, 399
Kaufman M. J., Wolfire M. G., Hollenbach D. J., Luhman M. L., 1999, ApJ, 527, 795
Kennicutt, Jr. R. C., 1998, ApJ, 498, 541
Kritsuk A. G., Norman M. L., Wagner R., 2011, ApJL, 727, L20
Krčo M., Goldsmith P. F., Brown R. L., Li D., 2008, ApJ, 689, 276

Le Petit F., Nehmé C., Le Bourlot J., Roueff E., 2006, ApJS, 164, 506
Lee D.-H. et al., 2006, ApJL, 644, L181
Li D., Goldsmith P. F., 2003, ApJ, 585, 823
Li W., Evans, II N. J., Jaffe D. T., van Dishoeck E. F., Thi W.-F., 2002, ApJ, 568, 242
Loinard L., Mioduszewski A. J., Torres R. M., Dzib S., Rodríguez L. F., Boden A. F., 2011, in Revista Mexicana de Astronomia y Astrofisica Conference Series, Vol. 40, Revista Mexicana de Astronomia y Astrofisica Conference Series, pp. 205–210
Loinard L., Torres R. M., Mioduszewski A. J., Rodríguez L. F., González-Lópezlira R. A., Lachaume R., Vázquez V., González E., 2007, ApJ, 671, 546
Murthy J., Sahnow D. J., 2004, ApJ, 615, 315
Narayanan G., Heyer M. H., Brunt C., Goldsmith P. F., Snell R., Li D., 2008, ApJS, 177, 341
Nguyen Luong Q. et al., 2011, A&A, 529, A41
Passot T., Vázquez-Semadeni E., 1998, Phys. Rev. E, 58, 4501
Peek J. E. G. et al., 2011, ApJS, 194, 20
Pineda J. L., Goldsmith P. F., Chapman N., Snell R. L., Li D., Cambrésy L., Brunt C., 2010, ApJ, 721, 686
Röllig M. et al., 2007, A&A, 467, 187
Röllig M., Ossenkopf V., Jeyakumar S., Stutzki J., Sternberg A., 2006, A&A, 451, 917
Schlegel D. J., Finkbeiner D. P., Davis M., 1998, ApJ, 500, 525
Smith D. A., Allen R. J., Bohlin R. C., Nicholson N., Stecher T. P., 2000, ApJ, 538, 608
Sternberg A., 1988, ApJ, 332, 400
Torres R. M., Loinard L., Mioduszewski A. J., Rodríguez L. F., 2007, ApJ, 671, 1813
Torres R. M., Loinard L., Mioduszewski A. J., Rodríguez L. F., 2009, ApJ, 698, 242
Ungerechts H., Thaddeus P., 1987, ApJS, 63, 645
van Dishoeck E. F., Black J. H., 1986, ApJS, 62, 109
Vázquez-Semadeni E., 1994, ApJ, 423, 681
Vázquez-Semadeni E., González R. F., Ballesteros-Paredes J., Gazol A., Kim J., 2008, MNRAS, 390, 769
Wolfire M. G., Hollenbach D., McKee C. F., 2010, ApJ, 716, 1191
Wolfire M. G., Hollenbach D., Tielens A. G. G. M., 1993, ApJ, 402, 195